Phase-contrast microscopy at high x-ray energy with a laboratory setup

Marco Endrizzi,[1,*] Fabio A. Vittoria,[1,2] Paul C. Diemoz,[1,2] Rodolfo Lorenzo,[3] Robert D. Speller,[1] Ulrich H. Wagner,[4] Christoph Rau,[4] Ian K. Robinson,[2,5] and Alessandro Olivo[1,2]

[1]*Department of Medical Physics and Bioengineering, University College London, Gower Street, WC1E 6BT London, UK*

[2]*Research Complex at Harwell, Harwell Oxford Campus, OX11 0FA Didcot, UK*

[3]*Department of Civil Engineering, University College London, Gower Street, WC1E 6BT London, UK*

[4]*Diamond Light Source, Harwell Oxford Campus, OX11 0DE Didcot, UK*

[5]*London Centre for Nanotechnology, WC1H 0AH London, UK*

Corresponding author: m.endrizzi@ucl.ac.uk

We report on the design and realization of an x-ray imaging system for quantitative phase-contrast microscopy at high x-ray energy with laboratory-scale instrumentation. Phase and amplitude were separated quantitatively at x-ray energies up to 80 keV with micrometric spatial resolution. The accuracy of the results was tested against numerical simulations, and the spatial resolution was experimentally quantified by measuring a Siemens star phase object. This simple setup should find broad application in those areas of x-ray imaging where high energy and spatial resolution are simultaneously required and in those difficult cases where the sample contains materials with similar x-ray absorption.   © 2014 Optical Society of America

OCIS codes: (110.7440) X-ray imaging; (180.7460) X-ray microscopy.

http://dx.doi.org/10.1364/OL.39.003332

Hard x-ray radiation has a high penetration power in matter, thus enabling nondestructive inspection of the inner structure of samples. At the same time, this power is also a weakness because the contrast arising from differences in the absorption of radiation tends to vanish when partially transparent samples are illuminated. X-ray phase-contrast imaging (XPCi) [1] overcomes this problem because it is sensitive to the phase shifts imparted to the x-ray wave when traversing the sample. Several methods [2–15] have been developed for performing XPCi. Approaches have also been proposed for high-resolution XPCi, including free-space propagation, Zernike phase contrast, and grating-based methods [16–22]. Here we show the design, modelling, and realization of a laboratory system based on the edge-illumination [10,15] principle and implemented through its area-imaging counterpart, sometimes referred to as the coded-aperture [23] method. These are noninterferometric methods that do not use the Talbot self-imaging effect or Moire patterns [24]; contrast is generated by fine angular selection, in analogy with analyzer-based imaging which uses the rocking curve of a crystal [25]. We aim to push the current resolution limits of a few tens of micrometers [26] toward microscopic resolution while still performing quantitative phase-contrast imaging at high x-ray energies. A magnified projection geometry was used in order to achieve high spatial resolution while being able to efficiently detect the radiation. The ability of the method to be quantitative and its spatial resolution are experimentally demonstrated and numerically simulated while the potential of the technique in terms of image quality is illustrated through images of a complex wood sample.

The experimental setup consists of a microfocus transmission target x-ray tube, two apertured masks, and a detector (Fig. 1). The tungsten target x-ray tube is operated at 80 kVp and has a focus of 3.5 μm. The first mask

M_1 is placed at 13 cm from the focus and the source-to-detector distance is $z_{sd} = 130$ cm. The sample is positioned at about 14 cm from the focus, with a geometrical magnification factor $G = z_{sd}/(z_{sd} - z_{od})$ of about 9. The first mask M_1 has a pitch $p_1 = 20$ μm and apertures $a_1 = 3$ μm, while $p_2 = 98$ μm and $a_2 = 29$ μm are used for the second mask M_2. They are made of gold on a graphite (M_2) and silicon (M_1) substrate and were manufactured by Creatv Microtech (Potomac, Maryland) and Microworks GmbH (Karlsruhe, Germany), respectively. The detector is a passive pixel complementary metal-oxide semiconductor flat panel sensor (Hamamatsu Photonics C9732DK), with pixel pitch $p_3 = 50$ μm. The signal degradation due to cross talk between neighboring pixels is limited by the use of a line-skipped mask design [27]. The main limiting factor for the field of view is a_1, which defines the angular acceptance of the transmitted radiation $\theta_m \approx a_1/t_{M_1}$, where t_{M_1} is the thickness of the mask, about 200 μm in this case. For our setup the field of view was 2 mm × 5 mm in the x and y directions, respectively.
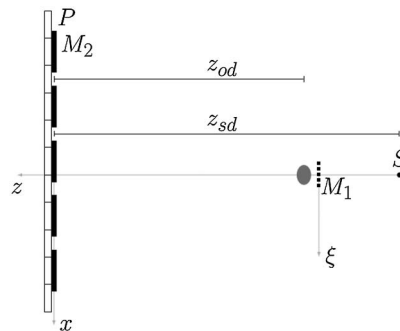

Fig. 1. Experimental setup: the x-ray beam, generated by a microfocus x-ray source S, is shaped by the first mask M_1, traverses the sample, and is analyzed by the second mask M_2 before being recorded by the pixels P of a digital detector.

Bent masks could be used for obtaining a larger field of view with an even more compact setup [28]. Provided that the angular spread of the beam is limited to $\theta_l < 8p_3/z_{od} \sim 340$ µrad, the pixels can be considered independent from one another, which allows us to model the image formation for a single aperture only.

Let us consider the Fourier transform of the intensity $I_D(x) = \int df \, \exp(2\pi i x f) \hat{I}_D(f)$ on the detector [29]:

$$\hat{I}_D(f) = \int dx' e^{-2\pi i x' f} T(x' - w) T^*(x' + w), \qquad (1)$$

where $w = z_{od}\lambda f/(2G)$ and $T(x) = A(x)\exp[-M(x)]\exp[-i\phi(x)]$ combines the aperture transmission function $A(x)$ and the sample absorption and phase shift. If not differently specified, the integration is always carried out between $-\infty$ and ∞. The signal detected is given by $S = \int_0^{a_2} dx I_D(x) \approx \int_0^\infty dx I_D(x)$ assuming a_2 is wider than the beam extension. Using $\int_0^\infty dx \, \exp(2\pi i x f) = (1/2)\delta(f) - [1/(2\pi i f)]$, where $\delta(f)$ represents the Dirac delta function, S can be expressed as a sum of two terms, $S = S_1 + S_2$. $S_1 = \int dx' |T(x')|^2$ and

$$S_2 = -\int dx' \int df \frac{e^{-2\pi i x' f}}{2\pi i f} T(x' - w) T^*(x' + w). \qquad (2)$$

The integration of S_2 can be split into two parts, $\int_{-\infty}^\infty df = \int_{-\infty}^0 df + \int_0^\infty df$, and rearranged into a single integral according to the properties of symmetry possessed by the integrand. The first term S_1 depends only on absorption while the second one S_2 is also related to phase. This can be shown explicitly by assuming constant absorption within the limits defined by the sample aperture and considering $|\phi(x' + w) - \phi(x' - w)| \ll 1$ [30]. The following form for S_2 is obtained:

$$S_2 = \frac{e^{-2M}}{\pi} \int_0^{\frac{a_1}{2}} dw \int_{-b_1}^{b_1} dx' \frac{\Delta\phi_{x'w}}{w} \cos\left[4\pi \frac{x'wG}{\lambda z_{od}}\right], \qquad (3)$$

where $\Delta\phi_{x'w} = \phi(x' - w) - \phi(x' + w)$, $b_1 = (a_1 - 2w)/2$, and the limits of integrations have been redefined according to the transmission function of the sample aperture. This expression provides a means to study how the phase signal is modulated by the imaging system. The component of the signal related to the phase effects is given by the weighted sum of all the possible difference quotients within the limits defined by the aperture. The weak phase condition used to derive Eq. (3) is required only to obtain a formulation easier to interpret, without the need to carry out the full integration numerically. In order to visualize this, the S_2 signal was calculated for a sinusoidal phase object, and its maximum value was plotted against the period in Fig. 2. It is interesting to note that the modulation is peaked at 3 µm, which corresponds to a_1, and also that signals with period smaller than the aperture are detected; for example, S_2 is reduced by about 50% at 1.5 µm.

The direct comparison between the measured and the theoretical signal from a star pattern test object is carried out by means of a numerical simulation of the whole imaging system [31]. Each monochromatic component was
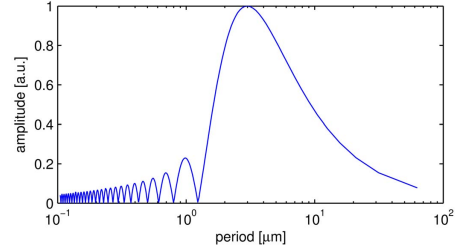

Fig. 2. Evaluation of Eq. (3) as a function of the period of a sinusoidal phase object.

weighted according to the x-ray source spectrum and the detector response as function of energy [32]. In order to perform quantitative retrieval of the absorption and refraction of the sample, we followed the approach based on the knowledge of the translation curve (TC) of the system [25]. The TC describes how the detected intensity changes as a function of the displacement $\Delta\xi$ between the two masks. Images were acquired by setting the displacement between M_1 and M_2 as equal to $\Delta\xi_1 = -\Delta\xi_2 = 2$ µm. The resulting images can be expressed as [25]

$$I_{L,R} = \exp\left[-\int_{\mathcal{O}} \bar{\mu} dz\right] I_{TC}(\Delta\xi_{1,2} - z_{od}\bar{\phi}_x/G), \qquad (4)$$

where $\bar{\mu}$ denotes the linear attenuation coefficient of the sample evaluated at the effective energy of the system [33], z_{od} is the sample-to-detector distance, $\bar{\phi}_x = \partial\bar{\phi}/\partial x$ is the partial derivative of ϕ at the effective energy of the system, and I_{TC} is the value of the translation curve. We also introduce the following images, $I_\Sigma = I_L + I_R$ and $I_\Delta = I_L - I_R$ [25]. It is worth noting that the quantity I_Δ/I_Σ depends only upon $\bar{\phi}_x$ and the operational parameters of the setup [25]; we will refer to this quantity as the differential phase image. Moreover, I_Σ depends only on the absorption properties of the sample. The following samples were imaged experimentally: a star pattern, a cylindrical two-material sample, and a bamboo wood sample. The star pattern was etched into a few hundred micrometers of crystalline silicon and provides a good approximation of a pure phase object at the x-ray energies we used. The I_L image was acquired by using 100 sample scan steps of 0.2 µm, with an exposure time of 70 s per step. The cylindrical sample was composed of two materials, 220 µm diameter of boron with a 14 µm diameter tungsten core, and it was scanned with 16 steps of 1.2 µm, 100 s exposure time each. The bamboo wood was sliced to a thickness of about 500 µm; I_L and I_R were acquired by scanning the sample with 44 steps of 0.5 µm, with an exposure time of 100 s per step. For comparison, an image of the bamboo sample was also acquired in free-space propagation XPCi, with monochromatic synchrotron radiation and a high-resolution detector. The image was acquired at the I13 beamline of the diamond light source by using 9.7 keV x-rays and a detector featuring 0.8 µm size pixels. The sample was placed at about 200 m from the undulator source and the detector 30 cm downstream of the sample.

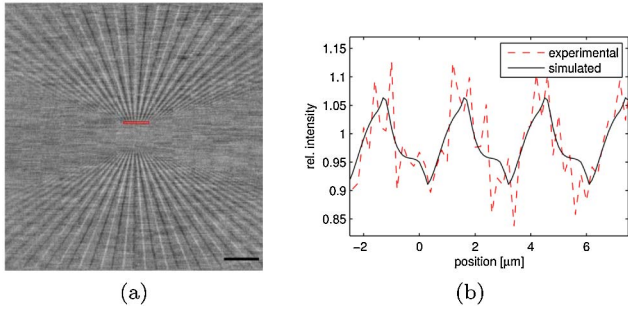The spatial resolution of the laboratory-based system is evaluated by means of the star pattern. The image of

Fig. 3. Star pattern phase object. (a) Differential phase-contrast experimental image (scale bar is 50 μm). (b) Simulation (solid line) compared against the experimental profile (dashed line) extracted from the highlighted region in the center of the star.

Fig. 5. Image of the bamboo sample. (a) Differential phase and (b) amplitude images, quantitatively separated by using the laboratory setup (scale bar 100 μm). (c) Zoom of the highlighted 120 μm × 120 μm regions of (a) and (b), top and bottom, respectively. (d) Free-space propagation image acquired with a high-resolution detector and monochromatic synchrotron radiation.

the star is shown in Fig. 3(a) from which the intensity profile shown in Fig. 3(b) was extracted (dashed line). The experimental data are in good agreement with the numerical simulation, shown as a solid line in the plot in Fig. 3(b). As the absorption is negligible in this case, we note from Eq. (4) that I_L depends only on $\bar{\phi}_x$ and on the operational parameters of the setup. The changing visibility of the phase-contrast features around the star pattern are a property of the geometry of the setup. Let us consider the phase shift of the star pattern as a replica at various angles φ of a step-like feature; the detected signal is modulated by a cosine function, $S_2 \propto \cos(\varphi)\partial_u\phi(u, v)$, where (u, v) are the (x, y) coordinates rotated by the angle φ. The smallest resolved separation between a dark and a bright fringe is 1.5 μm; the sample used hardly allowed testing finer resolutions. The quantitativeness of the method is demonstrated by retrieving differential phase and amplitude of the boron fiber with a tungsten core and comparing the extracted (dashed line) values to the expected ones (solid line) in Fig. 4(a). The theoretical $\bar{\phi}_x(x)$ was calculated assuming a cylindrical shape of the boron and tungsten fiber. The analytical profile was convolved with a Gaussian function, representing the spatial resolution of the system, of width 1.5 μm. The refractive indices of the materials were calculated by using the Xraylib library [34]. The profile was then obtained according to $I_\Delta/I_\Sigma = (z_{od}\bar{\phi}_x/G)/(I'_{TC}(\Delta\xi)/I_{TC}(\Delta\xi))$ [25] by numerically differentiating $\bar{\phi}$. The amplitude and differential phase images

are also shown in Figs. 4(c) and 4(b), respectively. The horizontal line noise that can be noticed in Figs. 3(a), 4(b), and 4(c) is a result of the brick-like structure used to manufacture M_1. The laboratory images of the bamboo sample are shown in Fig. 5, where the contributions from phase [Fig. 5(a)] and absorption [Fig. 5(b)] are separated. For a better appreciation of the image quality, the image acquired under nearly ideal conditions (with monochromatic synchrotron radiation and high-resolution detector) is also shown for comparison in Fig. 5(d). We note that the higher contrast of this image is expected due to the much lower x-ray energy (9.7 keV). The detail shown in the picture is similar to but not exactly the same as in the laboratory image, due to difficulty in aligning the sample to the same region of interest.

In summary, we described a hard x-ray, laboratory-based, phase-contrast microscope, obtained through the appropriate design of a high-magnification edge-illumination XPCi system. The experimental setup was built using commercially available, off-the-shelf instrumentation, and it is currently producing high-quality amplitude and differential phase-contrast images. Micrometric spatial resolution was experimentally measured, theoretically described, and numerically simulated by using a star pattern test object, with good agreement between simulation and experiment. By acquiring two separate images at different configurations, amplitude and differential phase can be quantitatively retrieved. The quantitativeness of the method was tested against theory on a two-material sample of known shape and composition. The instrument uses broadband and hard radiation, merging high resolution with the high penetration power of x-rays in a laboratory setup.
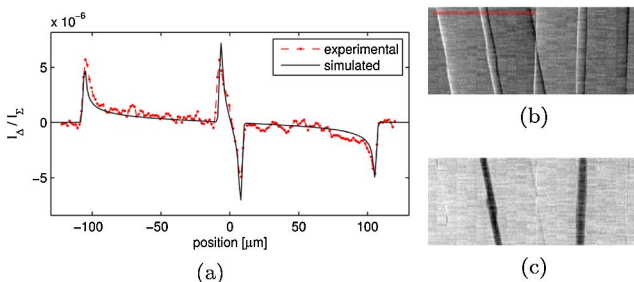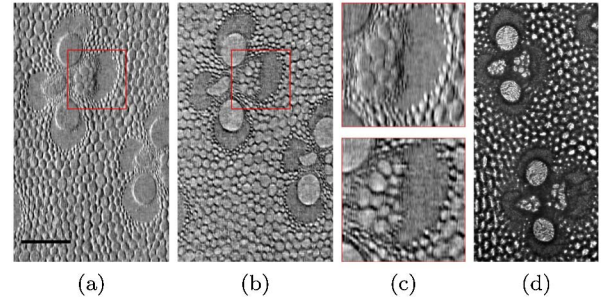
Fig. 4. Boron fiber with a tungsten core sample. (a) Comparison of the experimental intensity profile [highlighted region in (b) sector] against the theoretically expected one for a single fiber. (b) Differential phase and (c) amplitude images of two fibers at an angle.

References

1. R. Fitzgerald, Phys. Today **53**(7), 23 (2000).

2. U. Bonse and M. Hart, Appl. Phys. Lett. **6**, 155 (1965).
3. K. Goetz, E. Foerster, P. Zaumseil, M. P. Kalashnikov, I. A. Mikhailov, G. V. Sklizkov, and S. I. Fedotov, Kvantovaia Elektronika Moscow **6**, 1037 (1979).
4. E. Foerster, K. Goetz, and P. Zaumseil, Kristall und Technik **15**, 937 (1980).
5. V. N. Ingal and E. A. Beliaevskaya, J. Phys. D **28**, 2314 (1995).
6. A. Snigirev, I. Snigireva, V. Kohn, S. Kuznetsov, and I. Schelokov, Rev. Sci. Instrum. **66**, 5486 (1995).
7. T. J. Davis, D. Gao, T. E. Gureyev, A. W. Stevenson, and S. W. Wilkins, Nature **373**, 595 (1995).
8. S. W. Wilkins, T. E. Gureyev, D. Gao, A. Pogany, and A. W. Stevenson, Nature **384**, 335 (1996).
9. A. Momose, T. Takeda, Y. Itai, and K. Hirano, Nat. Med. **2**, 473 (1996).
10. A. Olivo, F. Arfelli, G. Cantatore, R. Longo, R. H. Menk, S. Pani, M. Prest, P. Poropat, L. Rigon, G. Tromba, E. Vallazza, and E. Castelli, Med. Phys. **28**, 1610 (2001).
11. C. David, B. Nohammer, H. H. Solak, and E. Ziegler, Appl. Phys. Lett. **81**, 3287 (2002).
12. T. Weitkamp, A. Diaz, C. David, F. Pfeiffer, M. Stampanoni, P. Cloetens, and E. Ziegler, Opt. Express **13**, 6296 (2005).
13. F. Pfeiffer, T. Weitkamp, O. Bunk, and C. David, Nat. Phys. **2**, 258 (2006).
14. Z.-F. Huang, K.-J. Kang, L. Zhang, Z.-Q. Chen, F. Ding, Z.-T. Wang, and Q.-G. Fang, Phys. Rev. A **79**, 013815 (2009).
15. P. R. Munro, K. Ignatyev, R. D. Speller, and A. Olivo, Proc. Natl. Acad. Sci. USA **109**, 13922 (2012).
16. S. Mayo, T. Davis, T. Gureyev, P. Miller, D. Paganin, A. Pogany, A. Stevenson, and S. Wilkins, Opt. Express **11**, 2289 (2003).
17. M. Engelhardt, J. Baumann, M. Schuster, C. Kottler, F. Pfeiffer, O. Bunk, and C. David, Appl. Phys. Lett. **90**, 224101 (2007).
18. Y. Takeda, W. Yashiro, T. Hattori, A. Takeuchi, Y. Suzuki, and A. Momose, Appl. Phys. Express **1**, 117002 (2008).
19. W. Yashiro, Y. Takeda, A. Takeuchi, Y. Suzuki, and A. Momose, Phys. Rev. Lett. **103**, 180801 (2009).
20. C. Holzner, M. Feser, S. Vogt, B. Hornberger, S. B. Baines, and C. Jacobsen, Nat. Phys. **6**, 883 (2010).
21. H. Kuwabara, W. Yashiro, S. Harasse, H. Mizutani, and A. Momose, Appl. Phys. Express **4**, 062502 (2011).
22. J. Choi and Y.-S. Park, Appl. Phys. Express **5**, 042503 (2012).
23. A. Olivo and R. Speller, Appl. Phys. Lett. **91**, 074106 (2007).
24. P. R. Munro, L. Rigon, K. Ignatyev, F. C. Lopez, D. Dreossi, R. D. Speller, and A. Olivo, Opt. Express **21**, 647 (2013).
25. P. R. Munro, C. K. Hagen, M. B. Szafraniec, and A. Olivo, Opt. Express **21**, 11187 (2013).
26. M. Marenzana, C. K. Hagen, P. D. N. Borges, M. Endrizzi, M. B. Szafraniec, K. Ignatyev, and A. Olivo, Phys. Med. Biol. **57**, 8173 (2012).
27. K. Ignatyev, P. R. T. Munro, R. D. Speller, and A. Olivo, Rev. Sci. Instrum. **82**, 073702 (2011).
28. T. Thuering, P. Modregger, T. Grund, J. Kenntner, C. David, and M. Stampanoni, Appl. Phys. Lett. **99**, 041111 (2011).
29. J. P. Guigay, C. R. Acad. Sc. Paris **284B**, 193 (1977).
30. J. P. Guigay, Optik **49**, 121 (1977).
31. F. A. Vittoria, P. C. Diemoz, M. Endrizzi, L. Rigon, F. C. Lopez, D. Dreossi, P. R. T. Munro, and A. Olivo, Appl. Opt. **52**, 6940 (2013).
32. M. Endrizzi, P. Oliva, B. Golosio, and P. Delogu, Nucl. Instrum. Methods Phys. Res. A **703**, 26 (2013).
33. P. R. T. Munro and A. Olivo, Phys. Rev. A **87**, 053838 (2013).
34. T. Schoonjans, A. Brunetti, B. Golosio, M. S. del Rio, V. A. Solé, C. Ferrero, and L. Vincze, Spectrochim. Acta B **66**, 776 (2011).